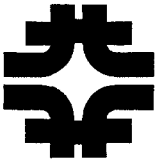

Fermi National Accelerator Laboratory

FERMILAB-FN-613

# The Antiproton Sources: Design and Operation

M.D. Church and J.P. Marriner

*Fermi National Accelerator Laboratory*
*P.O. Box 500, Batavia, Illinois 60510*

November 1993

Operated by Universities Research Association Inc. under Contract No. DE-AC02-76CHO3000 with the United States Department of Energy

## Disclaimer

# THE ANTIPROTON SOURCES: Design and Operation

*M. D. Church and J. P. Marriner*

Fermilab[1], P.O. Box 500, Batavia, Illinois 60510

KEY WORDS: antiproton production, antiproton accumulation, stochastic cooling, lithium lens, Schottky signals

---

CONTENTS



## 1. INTRODUCTION

In 1976 Rubbia, McIntyre & Cline (1) suggested that it would be practical to create high energy collisions by colliding beams of protons and antiprotons. At that time, colliding-beam techniques had proven practical in the successful operation of the Intersecting Storage Rings (ISR) at CERN (proton-proton collisions) and SPEAR at SLAC (electron-positron collisions). However, the highest energy beams available

[1] Operated by the Universities Research Association under contract no. DE-AC02-76CHO3000 with the US Department of Energy.

came from proton synchrotrons: the SPS at CERN and the (not yet completed) Tevatron at FNAL. A single ring can accommodate two counter-rotating beams, provided the beam particles have opposite charge. Thus, the SPS and the Tevatron, which were conceived for fixed-target experiments, could be utilized as colliding-beam machines if sufficiently intense antiproton beams could be produced. The great virtue of this scheme was that these synchrotrons could be converted into colliding-beam storage rings with minor modifications to the radiofrequency (rf) and injection systems. However, an intense antiproton source would be required in order to achieve adequate luminosity. It is the design and operation of these sources that are the subject of this review.

An adequate antiproton source could be realized only with the invention of beam-cooling techniques. Secondary beams of antiprotons are produced by targeting an intense proton beam. Secondary antiproton beams used by antiproton sources have, at best, five orders of magnitude less beam intensity than the proton beams used to produce them. Thus, in order to have antiproton beam intensities comparable to proton beams, it is necessary to accumulate $10^5$ pulses of secondary antiprotons. However, it is not enough merely to produce the $10^5$ pulses. The antiproton pulses are collected and accumulated in a storage ring with finite apertures that limit the size (or phase space) of the beam that can be stored. Using ordinary techniques, one cannot add new beam to a storage ring without displacing the beam already stored in that portion of the phase space. While antiproton collection systems do have somewhat larger apertures, they do not have $10^5$ more phase space. In order to accommodate the antiproton pulses, the beam phase space must be reduced by $10^5$ or more. The process of reducing the phase space area of each antiproton pulse as it is collected is the central problem that confronts an antiproton source.

The reduction of the phase space occupied by a particle beam is often referred to as beam "cooling." Two techniques are currently available for cooling high energy particle beams. Electron cooling was proposed by Budker (2) in 1966 and was demonstrated by Budker et al (3), in 1976. Stochastic cooling was discussed by van der Meer (4) in 1972. Electron cooling is most effective for beams of fairly small size, and it is quite effective with high density beams. Stochastic cooling is most effective for low density beams and works well with large beam sizes. Because of the low density and large beam size, stochastic cooling is used at the antiproton sources.

After its invention, stochastic cooling was demonstrated (5, 6) at the CERN ISR. Because cooling at the ISR took place with much denser

beams than would be the case at an antiproton source, additional experiments (7, 8) on stochastic cooling were performed in ICE (Initial Cooling Experiment).

There are two antiproton sources in existence. The original CERN antiproton source (9) (known as the AA, or antiproton accumulator) was commissioned in 1980. The AA was an essential component of the CERN accelerator complex that led to the award of the Nobel prize in 1984 to van der Meer and Rubbia for the discovery of the W and Z particles. The AA was later upgraded with the addition of a second ring, known as the AC, or antiproton collector (10). The Fermilab antiproton source (11) was commissioned in 1985 and currently serves as the antiproton injector for the highest energy accelerator in the world—the Tevatron.

The antiproton sources at CERN and FNAL are comparable in performance. Both sources accumulate antiprotons at a rate of about $4 \times 10^{10}\ \mathrm{hr}^{-1}$ (slightly higher at CERN, slightly lower at FNAL). The original AA was designed to accumulate antiprotons at a rate of $2.5 \times 10^{10}\ \mathrm{hr}^{-1}$, but only achieved $0.5 \times 10^{10}\ \mathrm{hr}^{-1}$. The subsequent AC upgrade, intended to increase the antiproton production rate by an order of magnitude, essentially achieved its design goal. The original FNAL design called for an accumulation rate of $10 \times 10^{10}\ \mathrm{hr}^{-1}$. The current FNAL accumulation rate has been achieved with modest upgrades that were not included in the original design. These upgrades have boosted the accumulation rate to its current value from a previous best of $2 \times 10^{10}\ \mathrm{hr}^{-1}$. A major factor in failing to reach the initial design goals was an overestimate (by a factor of about 2.5 at both CERN and FNAL) of the antiproton production cross section. However, both sources have increased their antiproton collection efficiencies to compensate partly for the lower cross sections.

While the original motivation in constructing the antiproton sources was to achieve high energy proton-antiproton collisions, the sources have been used for lower energy particle physics experiments as well. CERN constructed an additional storage ring to decelerate antiprotons for medium and low energy physics experiments. This storage ring is known as LEAR (12) (Low Energy Antiproton Ring). A major program of physics experiments continues to be performed at that facility, and the CERN antiproton source now operates only as the injector for LEAR. The antiproton source at FNAL has been used by a single dedicated experiment to study the production and decay of charmonium states produced by interactions of the stored antiproton beam and an internal gas jet target. Recently this experiment announced the discovery (13) of the $^1P_1$ state of the charmonium system. The prime

user of the FNAL antiproton source continues to be the high energy proton-antiproton Tevatron collider.

## 2. OVERVIEW OF THE ANTIPROTON SOURCES

The antiproton sources at FNAL and CERN are remarkably similar in design. The similarities are undoubtedly accentuated by the close cooperation that has existed between the two laboratories. The FNAL antiproton source design was strongly influenced by the success of the CERN AA. Early FNAL designs involving electron cooling were discarded in favor of the CERN AA, which used only stochastic cooling. On the other hand, FNAL pioneered the use of the bunch rotation technique and the lithium lens technology (14) developed at the Institute for Nuclear Physics at Novosibirsk.

Figure 1 shows the layout of the antiproton source at FNAL. A layout of the CERN source is shown in Figure 2. The description of the various components that follows is applicable to either source. The antiprotons are produced by targeting a primary proton beam on a target consisting of heavy nuclei. The proton beam is focused to a small size at the

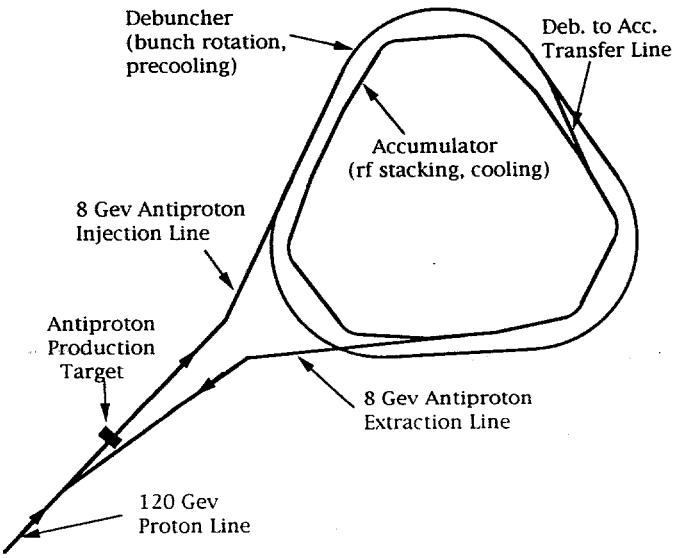


*Figure 1* The layout of the FNAL antiproton source is shown. Antiprotons are produced at the target by a 120-GeV proton beam and collected in the debuncher, where the bunches are rotated, debunched, and cooled. The antiprotons are then transferred and stored in the accumulator.

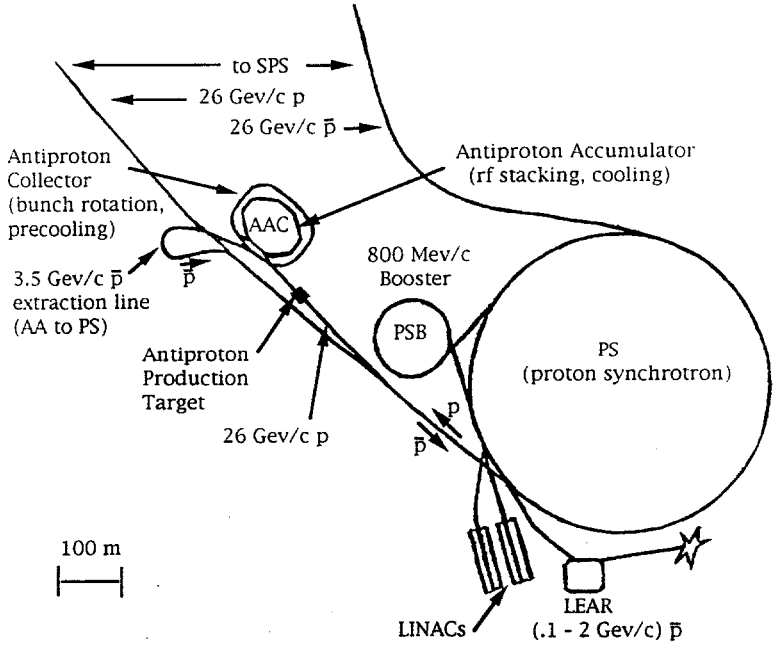


*Figure 2* The siting of the CERN antiproton source is shown. Antiprotons are produced by 26-GeV/*c* protons from the Proton Synchrotron (PS) striking a target near the Antiproton Accumulator Complex (AAC). The bunches are rotated and cooled in the antiproton collector (AC) and then transferred to the Antiproton Accumulator (AA). Antiproton beams from the AA may be transferred to the PS and then to LEAR or the Super Proton Synchrotron (SPS).

target. The small proton beam size maximizes the brightness of the secondary antiprotons and therefore increases the collection efficiency. The parameters of the proton beam are given in Table 1.

The secondary antiprotons are focused by a lithium lens and transported to a debunching and precooling ring. In the debunching ring the bunches, which inherit the narrow time spread from the proton beam, are debunched into a coasting beam. In this process, the narrow time spread and large momentum spread are traded for a large time spread and a narrow momentum spread. The beam is stochastically cooled following the bunch rotation. Table 2 lists some of the parameters for the debunching and cooling rings.

The beam is then transferred to an accumulation ring. The newly injected beam is added to the already stored beam by a process known as stochastic stacking. In this process, newly deposited beam is merged

**Table 1** Proton beam parameters

| Parameter | FNAL (main ring) | CERN (PS) |
|---|---|---|
| Momentum (GeV/$c$) | 120 | 26 |
| Protons per pulse | $1.8 \times 10^{12}$ | $1.5 \times 10^{13}$ |
| Cycle time (s) | 2.4 | 4.8 |
| Number of bunches | 84 | 5 |
| rf bucket length (ns) | 19 | 105 |
| rf bunch length (ns) | 1.5 | 30 |
| Beam radius ($\sigma$) at the target (mm) | 0.2 | 1.5 |

into the longitudinal phase space occupied by previous pulses, making room for the next pulse. The stored beam is cooled transversely to make the densest possible antiproton beam. When a sufficient number of antiprotons has been accumulated, beam is extracted from the accumulation ring and sent to the Tevatron, the SPS, or LEAR. The accumulation ring then returns to stacking, and, if things go well, there will be an adequate number of antiprotons stored in the accumulation ring before the next beam extraction. Table 3 lists some of the parameters of the accumulation rings.

## 3. INTRODUCTION TO PHASE SPACE

Phase space concepts are central to understanding the design of an antiproton source. A rudimentary summary of phase space concepts relating to accelerator physics is given here. Particles in a (stable) beam undergo oscillations around some reference orbit, say $x = p = 0$. For most purposes, these oscillations can be described by simple harmonic

**Table 2** Antiproton beam parameters in the debunching and precooling rings

| Parameter | FNAL (debuncher) | CERN (AC) |
|---|---|---|
| Momentum (GeV/$c$) | 8.9 | 3.57 |
| $\Delta p/p$ before rotation (%) | 4 | 6 |
| $\Delta p/p$ after rotation (%) | 0.2 | 1.5 |
| $\Delta p/p$ after cooling (%) | 0.1 | 0.18 |
| $\epsilon$ before precooling (mm-mrad) | $25\pi$ | $200\pi$ |
| $\epsilon$ after precooling (mm-mrad) | $3\pi$ | $5\pi$ |
| Stochastic cooling frequency band (GHz) | 2–4 | 1–3.2[a] |

[a] In three bands: 1–1.6, 1.6–2.4, and 2.4–3.2 GHz.

Table 3 Beam parameters in the accumulation rings

| Parameter | FNAL (accumulator) | CERN (AA) |
|---|---|---|
| Stacking rate ($hr^{-1}$) | $3.5 \times 10^{10}$ | $5 \times 10^{10}$ |
| $\bar{p}$ per pulse | $3 \times 10^{7}$ | $7 \times 10^{7}$ |
| Yield ($\bar{p}/p$) | $12 \times 10^{-6}$ | $5 \times 10^{-6}$ |
| Final $\Delta p/p$ (%) | 0.2 | 0.2 |
| Final emittance (mm-mrad) | $1\pi$ | $6\text{–}9\pi$ |
| Stack tail band (GHz) | 1–2 | 1–2 |
| Core cooling bands (GHz) | 2–4, 4–8 | 1–2, 2–4, 4–8 |
| Total number of antiprotons | $1 \times 10^{12}$ | $1 \times 10^{12}$ |
| Ring circumference (m) | 477 | 157 |

motion in a suitably chosen set of coordinates. For motion in a single dimension, the Hamiltonian of the simple harmonic oscillator is

$$H = \tfrac{1}{2} Ax^2 + \tfrac{1}{2} Bp^2. \qquad 1.$$

The quantity $H$ is conserved in simple harmonic motion, and therefore the trajectories of the particles can be described in terms of ellipses of constant $H$. A typical beam of particles will have a distribution of values of $H$ between zero and $H_{max}$. The value of $H_{max}$ is usually referred to as the emittance. A more convenient working definition often is the "95% emittance," the phase space area that contains 95% of the beam. All emittances quoted in this review may be understood as 95% emittances. Circular accelerators can be described in terms of the maximum emittance beam that can be circulated. This maximum emittance is called the acceptance.

To describe particle motion completely, one must, of course, include all three space dimensions. The usual description of particle trajectories is given in terms of horizontal and vertical displacements from some reference orbit. The conjugate momenta are the horizontal and vertical transverse momenta $p_H$ and $p_V$. The angles $\theta_H = p_H/p$ and $\theta_V = p_V/p$ are usually used in place of the momenta. The third coordinate may be chosen to be the time of arrival at some reference point; the conjugate momentum will be the particle energy. Both the time and energy are normally expressed as differences between the particle and a reference particle.

In the general case, motion in the three coordinates is coupled and the phase space is given by a six-dimensional ellipse. However, the antiproton sources are designed to have independent motion in each of the three coordinates. In practice, there is some coupling between

the coordinates, but it is not an essential feature in the antiproton sources; we neglect all coupling in the following discussion.

Thus, we can describe the motion of particles in terms of their sinusoidal oscillations in coordinate space or in terms of their elliptical trajectories in phase space. The area of the ellipses that contain 95% of the beam depends on the amplitude of the oscillations and is usually given in units of mm-mrad for the transverse emittances and in units of eV-s for the longitudinal emittance. A particularly useful choice of coordinates leads to the beta function description of storage rings and to the parameterization of emittance as

$$\epsilon = \beta\theta^2 + 2\alpha\theta x + \frac{1 + \alpha^2}{\beta} x^2. \qquad 2.$$

In this formalism $\beta$ and $\alpha$ vary along the longitudinal position $s$ of the beam line, but the emittance $\epsilon$ is invariant. The beta function $\beta(s)$ describes the aspect ratio of this phase space ellipse, and can be engineered to achieve particular values. A detailed discussion of the beta function is beyond the scope of this paper, but several excellent introductions are available (15).

## 4. PRODUCTION CROSS SECTION ($p + N \rightarrow \bar{p} + X$)

Antiprotons can be produced in any particle-particle collision that is sufficiently energetic to produce a proton-antiproton pair. However, the process is not very efficient, and it is important to produce as many antiprotons as possible. The highest production rates are obtained with the process:

$$p + N \rightarrow \bar{p} + X, \qquad 3.$$

where p is a sufficiently energetic proton, N is a target nucleon, $\bar{p}$ is the produced antiproton, and X is any allowed particle or combination of particles. The major advantage of using protons as the projectile is that high energy, high intensity (primary) beams are readily available.

A comprehensive study of the reaction and its features relevant to antiproton sources was made by Hojvat & van Ginneken (16). They parameterize the inclusive cross section for antiproton production as

$$(E/\sigma_{abs})(d^3\sigma/dp^3) = [0.065(1 - x_r)^8 \exp(-3p_t^2)][1 + 24s^{-2} \exp(8x_r)] \times [a \exp(bp_t^2) \exp(-cx_r)], \qquad 4.$$

where $p_t$ is the transverse momentum of the antiproton and $s$ is the

square of the center-of-mass energy. The quantity $x_r$ is the so-called radial scaling variable (17), $x_r = E_{\bar{p}}/E_{max}$, where the energies are expressed in the center-of-mass system and $E_{max}$ is the maximum antiproton energy that is kinematically allowed (ignoring Fermi motion in the target nucleus).

The parameterization in Equation 4 consists of three multiplicative factors: *(a)* the cross section for a hydrogen target at infinite energy, *(b)* a factor that describes deviations from scaling (this factor contains the $s$ dependence), and *(c)* a factor that describes the nuclear dependence. The first factor describes the most important features of antiproton production: the cross section is largest near $x_r = 0$ and $p_t = 0$. Note that $x_r = 0$ is not possible except as $s \rightarrow \infty$, since the minimum value is $x_r = m_p/E_{max}$. The approach to scaling factor is not very significant (1.13 at CERN and smaller at FNAL).

While the above parameterization can be quite useful for understanding the basic features of antiproton production, its accuracy should not be taken for granted. The scaling properties are only approximate over a limited range of the parameters, and the nuclear dependence of the cross section is not well established. Ultimately the validity of the parameterization rests on the quality of its agreement with the experimental data.

The yield is maximized at momenta corresponding to production at rest in the proton-nucleon center of mass. These momenta are 7.5 GeV/$c$ at FNAL (120 GeV/$c$ proton beam) and 3.4 GeV/$c$ at CERN (26 GeV/$c$ proton beam) and are rather close to the actual momenta of the collected antiprotons, namely 3.6 GeV/$c$ at CERN and 8.9 GeV/$c$ at FNAL. Around the nominal momentum, CERN collects a momentum spread of $\Delta p/p = 6\%$; FNAL collects $\Delta p/p = 4\%$. The variation of the cross section over these momentum ranges is small. More antiprotons could be collected with larger momentum acceptance. Most of the antiprotons are within $p_t < 300$ MeV/$c$ or laboratory angles of $300/3500 \approx 90$ mrad at CERN and $300/8900 \approx 30$ mrad at FNAL. Unfortunately, even with the optimum parameters, the yield of antiprotons is pitifully small: the number of antiprotons collected per targeted proton is measured in parts per million.

It is therefore particularly important to identify the limitations to the number of antiprotons that are collected. Providing adequate angular coverage at the target is crucial but not sufficient. The antiproton beam transport line and collection ring will necessarily have focusing elements that will change angular displacements into position displacements and vice versa. Under these conditions, the most important beam parameter is neither the spread in positions nor angles but the phase

space occupied by the beam. The distribution in angles at the target is determined entirely by the production process. The distribution in position, however, is determined entirely by the size of the proton beam. Thus, the phase space of the antiproton beam is minimized by focusing the proton beam to the smallest possible size at the target.

A similar technique is applied to the longitudinal emittance, although the reason is somewhat different. The collection efficiency of the antiprotons depends largely on $\Delta p/p$ and is essentially independent of the spread in time. This is because there is no longitudinal focusing in the beam line and because longitudinal focusing in the collection ring requires many turns before it becomes established. However, a small longitudinal emittance is important in reducing the momentum aperture and the power requirements of the antiproton stacking system. For this reason the longitudinal emittance is minimized by producing antiprotons with bunches of protons having the narrowest possible time spread and accepting as large a momentum spread as possible.

## 5. TARGET TECHNOLOGY

The most difficult technical issues concerning targeting arise from the energy deposited in the target by the beam. As discussed in the next section, the phase space density of the antiproton beam is maximized by using the shortest possible target. Thus, targets of heavy nuclei are preferred. However, the increase in antiproton yield will not be useful if the increased energy deposition in the high-$Z$ targets causes a structural failure in the target. A detailed calculation (18) shows that for a 7-cm Cu target ($Z = 29$) the average total energy deposited by a 120-GeV/$c$ proton is 1.34 GeV, of which about 67% is from electromagnetic showers (19). For a 5-cm tungsten ($Z = 74$) target the energy deposition is 10.98 GeV and 85% is electromagnetic. For targeting at FNAL ($2 \times 10^{12}$ protons at 120 GeV/$c$ every 2.4 s) an average power of 360 W must be dissipated. At CERN ($1 \times 10^{13}$ protons at 26 GeV/$c$ every 4.8 s into tungsten-rhenium) the average power is near 1200 W. These power levels are significant, but not extraordinary.

A problem does arise, however, because the energy is deposited over a very small volume. A more relevant quantity, therefore, is the maximum energy density, $E_m$. Figure 3 shows a plot of $E_m$ vs rms beam spot size (20) for the FNAL beam parameters. CERN targets more beam into a larger area, but the energy density is similar to that at FNAL. One can see that the maximum energy density increases rapidly as spot size decreases, but recall that it is important to minimize the proton beam size in order maximize the antiproton phase space density. For typical FNAL targeting (spot size = 0.15 mm radius) $E_m$ is cal-

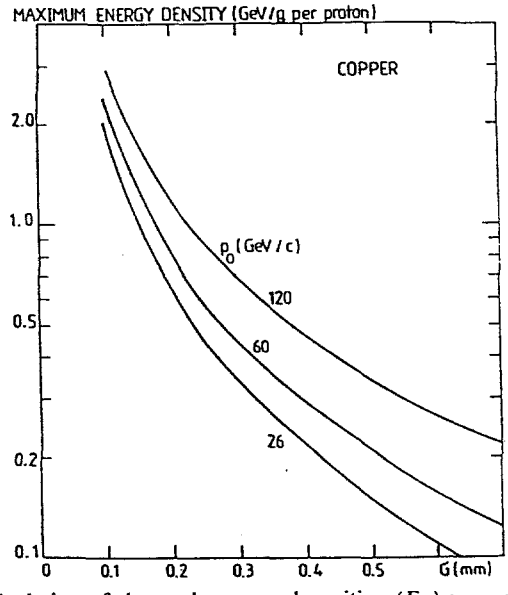


*Figure 3* A calculation of the peak energy deposition ($E_m$) vs proton beam size in millimeters ($\sigma$) is shown for a copper target.

culated to be 560 J/g. The local temperature increase due to this energy deposition can be easily determined if one neglects the small effects of heat conduction during the pulse and pressure variations. The energy deposition is related to the temperature increase by

$$\Delta E = \int_{300}^{T} C_v \, dT', \qquad 5.$$

where $C_v$ is the heat capacity at constant volume. For $E_m = 563$ J/g in copper, the temperature reaches 1700 K and the copper begins to melt. Thus, the FNAL copper target apparently operates close to the melting point.

After many pulses accompanied by cycles of local melting and solidification, one would expect a target to be permanently altered. In addition, one would see a drop in antiproton yield because the target density would decrease as a consequence of partial melting during the proton beam pulse. An attempt has been made to measure a possible density decrease in the FNAL Cu target by measuring the relative antiproton yields from the beginning and the tail of the 1.6-$\mu$s long proton pulse train (21). No effect was observed at the level of 5%.

Local energy deposition will also cause large pressure variations within a target, resulting in shock waves. Under the same assumptions

mentioned above, the maximum pressure increase in a target can be calculated (22) as a function of energy deposition from Gruneison's equation:

$$P = \rho\gamma E, \qquad 6.$$

where $\rho$ is the density and $\gamma$ is Gruneison's constant. For the FNAL Cu target, pressures at the beam position reach 7 GPa. It is very difficult to assess or control the potential shock-wave damage in a realistic target. After repeated pulses, deformation may cause loss of material strength, microfractures, or surface ruptures.

The conflicting requirements for a practical target—high $Z$ for high phase space density, high melting point, and low Gruneison's constant to withstand melting and thermal shock—have led to the investigation of a number of different target materials. FNAL has traditionally used a copper target. Copper is a compromise because it does not have the short absorption length of the very heavy metal targets. However, it does have excellent thermal properties, the modest $Z$ limits the energy deposition compared to heavier metals, and the magnitude of the shock wave is lower than that in most other materials. More recently nickel ($Z = 28$) and rhenium ($Z = 75$) in powdered and recompacted form have been used at FNAL. CERN has used copper, tungsten-rhenium, and, more recently, iridium targets. The CERN tungsten-rhenium target reflects a novel approach (23) in which graphite discs act as bumpers to absorb the shock wave. All these targets have been used without difficulty. However, in short test runs at FNAL, a tantalum target suffered severe swelling believed to be due to radiation damage, and a tungsten target cracked because of excessive temperature and/or pressure.

Experiments at FNAL (24) have been performed with a number of target materials. The FNAL target consists of a stack of discs of different materials. By raising and lowering the target it is possible to change the target material, and by moving the target horizontally, it is possible to change the target thickness presented to the beam. These experiments have measured the relative $\bar{p}$ yields of Al-Cu-W targets with the result Al:Cu:W = 0.41:0.93:1.00. These measurements appear to disagree with the parameterizations of the cross section (16, 19), which predict a ratio Cu:W = 0.80:1.00.

## 6. LITHIUM LENS

The type of focusing required for the antiprotons is determined by the distribution of particles in phase space, which can be calculated via

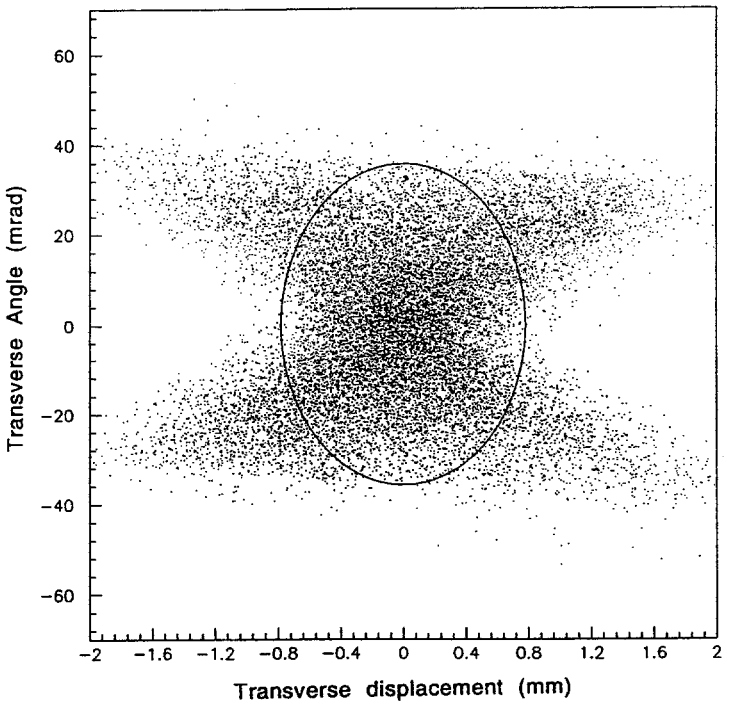


*Figure 4* The phase space distribution of antiprotons at the center ($z = 0$) of the FNAL target is shown. Only the particles within the lithium lens acceptance of roughly 35 mrad are plotted. The ellipse indicates the portion of phase space that is accepted by the $28\pi$ mm-mrad acceptance FNAL debuncher ring.

Monte Carlo techniques. Figure 4 shows the calculated distribution in transverse phase space at the target center ($z = 0$) for the FNAL target. The main features of this plot are determined by geometry and by the fact that the incoming proton beam has very small transverse dimensions. A particle produced at $x = 0$ and at $z = 0$ with a production angle $\theta_x$ will project to $z = 0$ with an $x = -z\theta_x/2$. For any given $\theta_x$, the values of $x$ will be $|x| < z_t\theta_x/2$, where $z_t$ is the length of the target. This naive prediction is exhibited by the simulation, but is smeared by the addition of a nonzero proton beam size and scattering in the target. The density falls rapidly with increasing angle because of the decrease in cross section with increasing $p_t$ and because the particles that are produced are spread over a greater range in $x$. The points plotted are for particles that would be accepted by a lens with a radius of 1 cm.

The ellipse plotted on Figure 4 shows which particles are contained in an acceptance of $28\pi$ mm-mrad, which is approximately the accep-

tance of the FNAL debuncher. The area of the ellipse is fixed by the debuncher aperture, but the aspect ratio may be varied by changing the beta function (see Equation 2). The aspect ratio of the ellipse drawn (0.8 mm × 36 mrad) was chosen to encompass the maximum number of particles. However, this aspect ratio for the phase space ellipse cannot be obtained with conventional magnets: 20 mm by 1.4 mrad would be more typical. In order to match to a conventional beam line, a lens capable of bending the largest angle antiprotons (35 mrad) to an angle of 0 ± 1 mrad is required. This lens must have adequate outer radius ($r_{max}$) to accept the beam divergence.

The geometry of the FNAL target station is shown schematically in Figure 5 along with some particle trajectories. In order to minimize the magnetic field required for a given value of $r_{max}$, the distance from the center of the target to the lens is chosen to be proportional to $r_{max}$. In this case, the maximum bend angle that the lens must provide is $\theta_b = -0.3GLr_{max}/p$, where $G$ is the lens gradient and $L$ is its length. With this scaling the maximum-angle antiproton accepted by the lens does not depend on $r_{max}$ except when $r_{max}$ is small and the difference in acceptance between the upstream and downstream ends of the target becomes important. A large $r_{max}$ results in extreme sensitivity to focusing errors. One such (unavoidable) error is the dependence of the

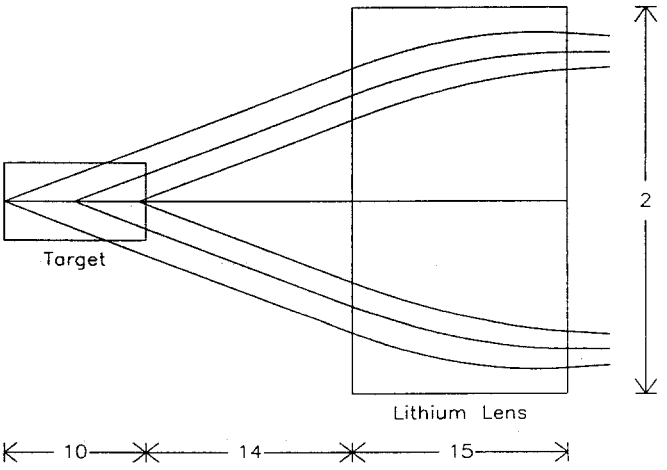


*Figure 5* The layout of the FNAL target station is shown schematically. The proton beam (not shown) is incident from the left. Several antiproton trajectories are shown emanating from the target. The target width is not accurately represented in this drawing. All dimensions are in cm.

bend angle on the momentum. Larger aperture devices also have more stored energy and tend to be undesirable for practical reasons. For a fixed $r_{max}$ the acceptance is maximized by making the lens short and pushing the gradient as high as technology will allow.

Both the CERN and FNAL source now use lithium lenses (25, 26) to accomplish the focusing function. Originally CERN had used a magnetic horn (27). A lithium lens is basically a cylindrical piece of lithium that has a very large axial current. The field produced by a steady current in the lithium is

$$B = \frac{\mu_0 J r}{2}, \qquad 7.$$

where $J$ is the current density and $r$ is the cylindrical radius at which the field is sampled. In fact, the current is pulsed, but Equation 7 is still approximately valid. The field is proportional to radius, which results in focusing. A lithium lens has an important advantage over conventional alternating gradient focusing: it can achieve a larger acceptance because both horizontal and vertical planes are focused in the same device. The disadvantage is that the beam must pass through the lithium. This disadvantage is mitigated by the choice of a material with long nuclear absorption and radiation lengths. The combination of nuclear, mechanical, and electrical requirements makes lithium uniquely suitable for such a lens.

Both the CERN and FNAL lithium lenses have a radius of 1 cm. A gradient of about 800 T/m is required for a 1-cm lens with the FNAL target geometry shown in Figure 5. This gradient requires a current density ($J$) of $1.3 \times 10^9$ A/m$^2$ and a total current of $4 \times 10^5$ A. It is not practical to deliver such high currents for an extended period of time, so the current is pulsed with a half-sine wave of duration approximately 0.33 ms. The time is long enough for the fields to penetrate the conductor but not so long that a prohibitive amount of energy is deposited into either the lithium lens or its electrical leads. It is important that the field be nearly proportional to radius in order to avoid higher order optical distortions. Proportionality can be very nearly achieved provided that the beam passes through the lens slightly after the peak in the half sine of current—at about 110°.

Lithium lenses are technically demanding from the standpoint of mechanical engineering. Magnetic body forces equal to $\mathbf{J} \times \mathbf{B}$ push inward radially and push outward axially on the end caps (where the current flows radially out to the leads). The heat dissipation from the ohmic losses in the lithium and other parts of the current path deposit about 10 kJ per pulse. This heat creates pressures of about 150 MPa

in the lithium. The heat deposited must be extracted through a shell of material (the "cooling jacket") that surrounds the lithium. Water is used to remove the heat from the cooling jacket. The cooling jacket isolates the water and the lithium to avoid the undesired chemical reaction $Li + H_2O \rightarrow LiH_2$. The cooling jacket must be thin (so the heat is removed from the lithium before the next pulse), it must be of high strength (to withstand stresses of about 500 MPa), and it must not react with the lithium. These seemingly contradictory requirements are satisfied with stainless steel at CERN and titanium at FNAL.

## 7. SCHOTTKY SIGNALS

Schottky signals are an important diagnostic tool for coasting beams in synchrotrons. An understanding of Schottky signals is fundamental to an understanding of stochastic cooling as well. In the following, Schottky signals are described theoretically. Examples of their use as a diagnostic tool can be found in several of the sections below. Schottky detectors constitute a particularly effective diagnostic tool because they are used to make passive (not destructive) measurements with high sensitivity on a signal that is always present.

Consider first a single particle that passes an electronic pickup at some point in the accelerator. The particle induces image charges on the insides of the walls of the accelerator vacuum chamber. This image current develops a voltage across any impedances that exist in the vacuum chamber, e.g. a beam current pickup. The physics of accelerator beam pickups has been discussed by Lambertson & Goldberg (28). The signal seen at the pickup is equal to the beam current times the pickup impedance:

$$\begin{aligned} V_L(t) &= Z_L I(t) \\ &= Z_L\, ef_0 \sum_{n=-\infty}^{\infty} \delta(t - nT + t_0), \end{aligned} \qquad 8.$$

where $e$ is the charge on a proton, $f_0 = 1/T$, and $T$ is the revolution period of the particle. The second line in Equation 8 is the mathematical statement that the current detected by the pickup is a series of Dirac delta functions of current at time $t_0$ plus or minus any number of revolution periods. The Fourier transform of Equation 8 is

$$\tilde{V}(\omega) = Z_L\, ef_0 \sum_{n=-\infty}^{\infty} \exp(i\omega t_0)\, \delta(\omega = n\omega_0), \qquad 9.$$

where $\omega_0 = 2\pi f_0$. The forms of Equations 8 and 9 assume an infinite pickup bandwidth; the effects of finite bandwidth may be included simply into Equation 9 by writing $Z_L = Z_L(\omega)$. Equation 9 shows explicitly that the frequency spectrum consists of a discrete set of lines at multiples of the revolution frequency.

When more than one particle is present, the voltages from the various particles must be added to find the total voltage. The $t_0$'s of the particles (see Equation 8) will be randomly distributed and thus the net voltage from a random distribution of particles will be zero. However, the power spectrum, which is proportional to the rms voltage deviations, is not zero. The power spectrum is defined as

$$P_L(\omega) = \tilde{V}^*(\omega)\tilde{V}(\omega)/Z_0, \tag{10.}$$

where $Z_0$ is some standard reference impedance—normally 50 $\Omega$. A beam with a density $dN/d\omega_0 = \Pi(\omega_0)$ has a power spectrum

$$P_L(\omega) = \frac{Ne^2Z_L^2}{Z_0} \sum_{n=-\infty}^{\infty} \left(\frac{\omega}{2\pi|n|}\right)^2 \frac{1}{|n|} \Pi\left(\frac{\omega}{|n|}\right). \tag{11.}$$

Since all the particles in a synchrotron beam must have similar revolution frequencies, the density $\Pi(\omega_0)$ is zero except for a narrow range of $\omega_0$. If $n$ is not too large, the power is concentrated in bands at harmonics of the average revolution frequency. These concentrations of power are usually referred to as Schottky bands. Equation 11 is written with the convention $-\infty < \omega < \infty$, but the positive and negative frequencies are not physically distinct. A spectrum analyzer would measure power at frequencies $n\omega_0$, where $n$ is any positive integer. The momentum distribution of the beam particles can be inferred from the measured distribution in revolution frequencies through the differential relationship

$$\frac{\Delta f}{f_0} = -\frac{\Delta T}{T} = -\eta \frac{\Delta p}{p}, \tag{12.}$$

where $\eta$ is a constant that is a property of the storage ring.

As an example, a beam of $10^8$ particles with a revolution frequency of 1 MHz will produce a power of $2.6 \times 10^{-16}$ W/MHz. The thermal fluctuations in a 50-$\Omega$ system produce noise levels of $k_b T_r W$, where $k_b$ is Boltzman's constant, $W$ is the bandwidth, and $T_r$ is the temperature. At room temperature, the noise in a 1-MHz bandwidth is $1.38 \times 10^{-23}$ W-s/K $\times$ 393 K $\times$ $10^6$ Hz/MHz = $5.4 \times 10^{-15}$ W/MHz. The Schottky signal should be readily observable on a spectrum analyzer if the signal-to-noise ratio is one or more. This condition is always satisfied if the

momentum spread and therefore the width of the Schottky band is sufficiently narrow. In our example, signals are observable for bands that satisfy $n\eta\Delta p/p < 0.05$.

It is possible to build beam pickups that are sensitive to the dipole moment of the beam, namely the beam current times its position displacement. In this case one observes a single-particle voltage

$$V_T(t) = Z_T I(t) A \cos(Q\omega_0 t)$$

$$= Z_T ef_0 \sum_{n=-\infty}^{\infty} \delta(t - nT + t_0) A \cos(Q\omega_0 t + \phi_0), \qquad 13.$$

where $Z_T$ is the transverse pickup impedance, $A$ is the amplitude of betatron oscillations, and $Q$ is the betatron tune (number of betatron oscillation cycles in one turn around the synchrotron). The Schottky signal power spectrum is given by

$$P_T(\omega) = \frac{Z_T^2}{Z_0} e^2 A_{\text{rms}}^2 \sum_{n=-\infty}^{\infty} \left[\frac{\omega}{2\pi(n - Q)}\right]^2 \left|\frac{1}{n - \xi/\eta}\right| \Pi\left(\frac{\omega}{n - Q}\right), \qquad 14.$$

where the chromaticity $\xi$ is defined by

$$\Delta Q = \xi \frac{\Delta p}{p}. \qquad 15.$$

Equation 14 assumes that the rms betatron amplitude $A_{\text{rms}}^2$ does not depend on the revolution frequency $\omega_0$. The power is concentrated at two sideband frequencies per revolution frequency harmonic, namely $\omega = (n \pm Q)\omega_0$. The widths of the two sidebands are affected differently by the chromaticity; the chromaticity may be inferred from the widths of the sidebands. The total power in these sidebands can be used to measure the rms betatron amplitude. In fact, using a slightly more general expression than Equation 14, one can use Schottky spectra to measure the beam emittance and chromaticity as a function of momentum (29).

## 8. BUNCH ROTATION

The large momentum spread of the antiprotons at the target is exchanged for a large time spread in the debunching ring by a technique known as bunch rotation. The Hamiltonian for longitudinal motion in

the presence of voltage gain $V \sin(\omega_r t)$ can be written as

$$H = \frac{\eta}{2\beta^2 E}(\Delta E)^2 + \frac{eV\omega_0}{\pi\omega_r}\sin^2\left(\frac{\omega_r\tau}{2}\right), \qquad 16.$$

where $\beta = v/c = pc/E$, $\Delta E$ is the energy difference, and $\tau$ is the time the particle arrives at the rf cavity relative to the synchronous particle (which always arrives when the rf cavity voltage is zero). This Hamiltonian has the same form as the one for the pendulum, and $H$ is a constant of the motion. If $H$ is small, the Hamiltonian reduces to the simple harmonic oscillator form (Equation 1), and the particles oscillate in phase space with a frequency known as the synchrotron frequency. For larger values of $H$, the nonlinearity of the sine function causes a reduction in the synchrotron frequency. A distribution of particles that depends only on $H$ (and not on $\Delta E$ or $\tau$ separately) is said to be matched to the rf voltage. The synchrotron motion of the individual particles will not change a matched distribution. The largest value of $H$ in the distribution is (up to a scale factor) the longitudinal phase space of the beam. For fixed $H$, the ratio of the maximum energy to time deviation may be varied by changing the voltage of the rf. If the voltage is changed slowly, the value of $H$ for each particle is conserved. The antiprotons enter the debunching ring with a large momentum spread and small time spread. In principle, these bunches could be captured into matched rf buckets by using a very large voltage, and the voltage could be adiabatically reduced to zero, which would result in a coasting beam with a small energy spread. However, the rf voltage requirements of this method are prohibitive. It is more practical to use a process known as bunch rotation, in which the beam distribution is not stationary.

The process of bunch rotation is illustrated in Figure 6. Figure 6*a* shows the phase space distribution for a single bunch with short time spread and large momentum spread as it is injected into the debunching ring. Figure 6*b* shows the distribution a quarter of a synchrotron period later with a large time spread and small momentum spread. At this point, the rf voltage is quickly reduced to a small value so that the rf voltage is matched to the beam distribution. The rf voltage can then be adiabatically reduced to zero so the bunches merge with each other (Figure 6*c*). The process maintains a constant phase space density, and the momentum spread is further diminished.

The preparation of the proton beam in the Main Ring at Fermilab before targeting is essentially the reverse of this process. After acceleration to the extraction energy, the proton bunches occupy a very small fraction of the phase space area within the rf bucket. At this point

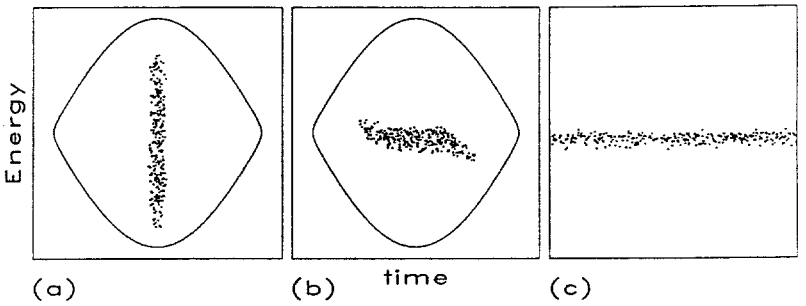


*Figure 6* This sequence of figures illustrates the process of bunch rotation. The bunches *(a)* initially have a small time spread and a large energy spread. The bunch distribution is mismatched to the bucket voltage and rotates a quarter turn *(b)* at the synchrotron frequency. After the quarter turn, the voltage is quickly reduced to capture the beam into a matched bucket, and then adiabatically reduced to zero to yield the unbunched distribution *(c)*.

the rf is quickly turned down so that the bunches shear in time. Then the rf voltage is quickly increased, and the bunches rotate 90° so that they occupy a narrow time spread. At this point the beam is extracted from the ring and delivered to the antiproton production target. Typical bunches are 1.5 ns wide and separated by 19 ns. The rf manipulations at the CERN proton synchrotron (PS) are more complicated because they also involve a bunch recombination scheme to achieve higher intensity (30).

In the Fermilab debuncher a 53-MHz, six-cavity rf system capable of 5-MV peak voltage is used for the bunch rotation (31) and a separate two-cavity 100-kV rf system is used for the adiabatic debunching. The rf voltage is kept at 5 MV for 50 $\mu$s, and then quickly turned down in 50 $\mu$s by reversing the phase of the power amplifier and driving the six high voltage cavities to 0 V. The two low voltage cavities adiabatically debunch the beam in 60 ms. The initial momentum distribution of 4% is reduced to about 0.3% as measured by the Schottky spectrum shown in Figure 7. At CERN a 1.2-MV 9.5-MHz two-cavity system (32) is used both to rotate and to adiabatically debunch the antiproton bunches. The voltage is held at 1.2 MV for 50 $\mu$s, driven down to 100 kV in 50 $\mu$s, and then adiabatically removed in 10 ms. The initial momentum spread of 6% is reduced to 1.5%.

Several factors limit the reduction in energy spread that can be obtained with bunch rotation. The most fundamental is the restriction that the phase space occupied by the beam may not be decreased. In addition, the variation of synchrotron frequency with amplitude (lower

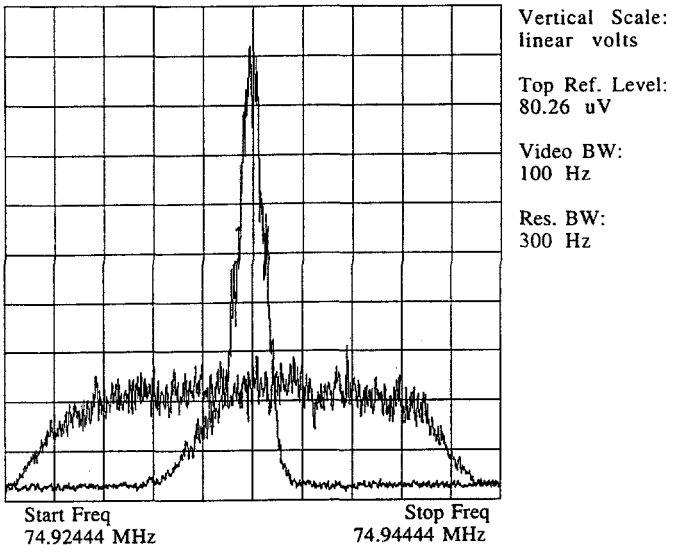


*Figure 7* Two spectrum analyzer traces show the effect of bunch rotation. The low flat trace shows a momentum spread of about 4% for the unrotated beam. The sharply peaked trace shows a momentum spread of about 0.3% after bunch rotation.

for large amplitude) gives rise to the peculiar "s" shape of the bunch seen in Figure 6*b* and results in a larger final momentum distribution. In order to reduce this nonlinearity, the rf bucket can be made larger by decreasing $|\eta|$ or by increasing the voltage (cf Equation 16). Practical restrictions on using higher voltages include cost, lack of space in the ring for more cavities, and technical difficulties in obtaining higher gradients. A smaller value of $|\eta|$ is unfavorable for the mixing factor (described in Section 9). Furthermore, exact linearity cannot be obtained with a very small $|\eta|$ because higher order terms (not shown in Equation 12) dominate as $|\eta|$ approaches zero.

## 9. BETATRON AND MOMENTUM STOCHASTIC PRECOOLING

Stochastic cooling has been described by a number of authors, including a comprehensive description by the early pioneers (33) and a more recent pedagogical approach (34). Antiproton sources require cooling of unbunched beams only, so here we do not consider the cooling of bunched beams. Stochastic cooling is easiest to conceptualize for the transverse degrees of freedom. Imagine a particle that

travels around a circular machine undergoing betatron oscillations with respect to the reference orbit. A schematic representation of a stochastic betatron cooling system is given in Figure 8. At the pickup electrodes, an electronic signal proportional to the displacement of the particle is detected. This signal is developed by taking the voltage difference between two electrodes on either side of the beam pipe. The signal, however, is very weak, with a voltage perhaps of the order of a nanovolt. It is amplified by some large factor (say $10^6$) and then applied to a kicker electrode. A kicker is the reciprocal of a pickup: it takes electric energy and converts it into beam motion. By positioning the kicker an odd multiple of 90° in betatron oscillation away from the pickup, the transverse electric and magnetic fields in the kicker can very slightly reduce (say one part in $10^6$) the angle corresponding to the position displacement at the pickup. This small effect quickly becomes significant for a beam that makes $10^6$ turns per second. The actual rate of the reduction of the amplitude, the amplification factor, and the power levels vary by several orders of magnitude depending on the system parameters.

When there is more than one particle in the accelerator, the situation is more complicated. We focus our attention on a single particle (the given particle) and consider the effects of the other particles. The small damping signal from the given particle is dwarfed in comparison with the signals from the other particles. The only reason that the single-

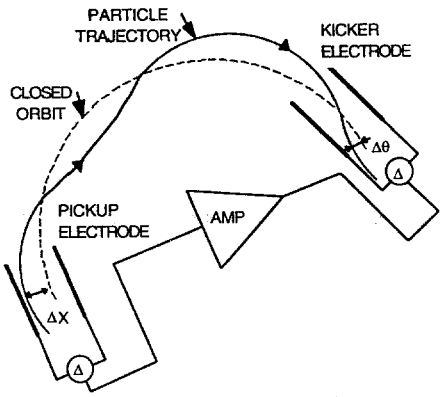


*Figure 8* A schematic of a typical betatron cooling system is shown. The particle displacement $\Delta x$ is detected at the pickup electrode. As the particle travels around the ring the betatron oscillations convert the position displacement to an angular displacement $\Delta\theta$. This angular displacement is reduced by the electric and magnetic fields that result from applying the amplified pickup signal to the kicker.

particle signal produces a significant effect is that the phases of other particles are randomly distributed, and the other particles are just as likely to decrease as to increase the amplitude of any given particle. To first order in the amplifier gain, the other particles produce no effect. However, the rms voltage of the other particles is large and causes the given particle to undergo a random walk in phase space. The rate of diffusion is proportional to the square of the noise voltage and therefore to the square of the amplifier gain. The effect of the particle on itself, which is proportional to the gain, dominates if the gain is sufficiently small.

To be more quantitative we must introduce two other features of the sampling process. The first important effect is the time resolution of the signal derived from the pickup. In principle, if the response of the pickup and the electronics were sufficiently fast, one could detect each particle individually. In this case, the signal of each particle would be isolated from every other particle and the Schottky noise from the other particles would not be of any consequence. Practical cooling systems fall far short of resolving individual particles, but by using a high bandwidth one can limit the number of other particles included with the particle of interest. The resolving time ($t_r$) of the system is related to the bandwidth ($W$) through the relationship $Wt_r \approx 1$. Practical stochastic cooling systems achieve bandwidths from hundreds of MHz to a few GHz.

The second particle sampling concept is the so-called mixing effect. Two particles that pass the pickup at the same time will initially be unresolved. However, because the particles have different revolution frequencies, they will be resolved after some number of turns $M$. Typical cooling systems operate with $M \approx 3$ although there is considerable variation. If $M$ is much smaller than three, the cooling effect tends to be diluted by excessive randomization of the particles between the time when the beam is sampled at the pickup and when it is corrected at the kicker. The randomization between pickup and kicker is sometimes called the "bad mixing," while the randomization between successive passes through the pickup is called "good mixing."

In addition to the Schottky noise from other particles, there is electronic noise in resistors and amplifiers. This noise is also amplified and applied as a correction to the beam. Putting all the effects into a simple formula, the cooling rate can be expressed as

$$\frac{d\epsilon}{dt} = \frac{W}{N}[-2g + (M + U)g^2]. \qquad 17.$$

The term proportional to $g$ is the cooling term. The term proportional

to $M$ describes the Schottky noise heating, and $U$ is the ratio of electronic noise power to Schottky beam power. In precooling systems $U$ may be the dominant noise source. A common technique to reduce the thermal noise is to cool to cryogenic temperatures the pickup resistors and the preamplifier (35). The cooling rate is optimized when $g = g_{opt}$, where

$$g_{opt} = \frac{1}{M + U}. \qquad 18.$$

At this optimum gain the cooling rate is

$$\frac{1}{\epsilon}\frac{d\epsilon}{dt} = -\frac{W}{N}\frac{1}{M + U}. \qquad 19.$$

The exact formulation of stochastic cooling phenomena (including a more precise definition of mixing effects, bandwidth effects, and phase errors) is most conveniently developed by making a Fourier transform into the frequency domain. One particularly important phenomena that is readily described in the frequency domain is the coherent response of the beam. One can think of the cooling system as a feedback system such as shown in Figure 9. The beam dipole signal $d_i(\omega)$ is input to the amplifier and a deflection $\Theta(\omega)$ is applied to the beam. This deflection causes a dipole moment of the beam, which adds to the dipole moment $d_i(\omega)$ from the Schottky signal. The observed signal $d(\omega)$ is given by

$$d(\omega) = \frac{d_i(\omega)}{1 - F(\omega)G(\omega)}, \qquad 20.$$

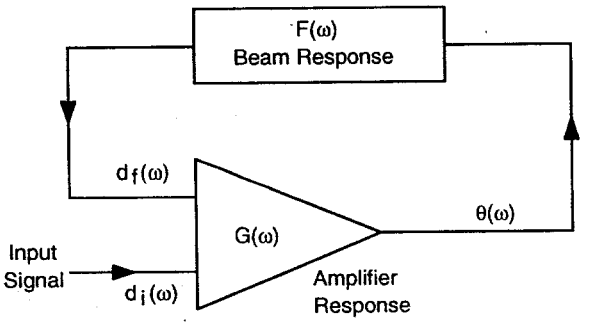


*Figure 9* Stochastic cooling can be modeled like more conventional feedback systems. The amplifier gain is $G(\omega)$ and the beam response is $F(\omega)$. The output results from the sum of two inputs: the input with feedback off ($d_i$) and the additional input ($d_f$) that results from the feedback.

where $F(\omega)$ is a function that describes the beam response and $G(\omega)$ is the gain of the cooling system. $F(\omega)$ will have a resonant response at betatron sidebands $(n \pm Q)\omega_0 t$. At the optimum cooling rate $G(\omega) = -1/F(\omega)$, i.e. the signal is reduced by a factor of two (33). This effect, called signal suppression, may be measured by observing the instantaneous reduction in the Schottky signal when the cooling system is turned on. Figure 10 is a particularly interesting example of signal suppression because the suppressed signal is reduced to a level below the thermal noise (base line away from the Schottky bands). In this case, the motion of the beam centroid partially cancels the thermal noise fluctuations in the amplifier.

If $G(\omega)$ is too large, has the wrong phase, or both, the cooling system may be unstable. A sufficient though not rigorously necessary condition for stability is that $\mathrm{Re}[F(\omega)G(\omega)] < 1$. Stability is not a problem theoretically except in the design of the momentum stacking system. In practice, systems may be unstable because of a wide variety of possible errors in achieving the desired gain function $G(\omega)$.

The feedback via the beam provides a powerful technique for measuring the cooling system in situ including the pickup and kicker responses. Such a measurement is shown for a Schottky band in Figure 11. The resonant structure is due to the beam response $F(\omega)$. Assuming $G(\omega)$ is constant over the Schottky band, its value can easily be determined by the peak responses from each of the Schottky bands. An

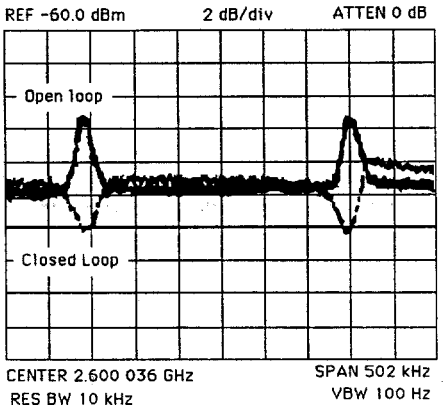


*Figure 10* A measurement of signal suppression in the FNAL debuncher: the top spectrum analyzer trace shows the Schottky signal with the cooling system off. The bottom trace is with cooling on. The peak difference between cooling on and off is about 6 dB, which indicates that the system gain is optimized.

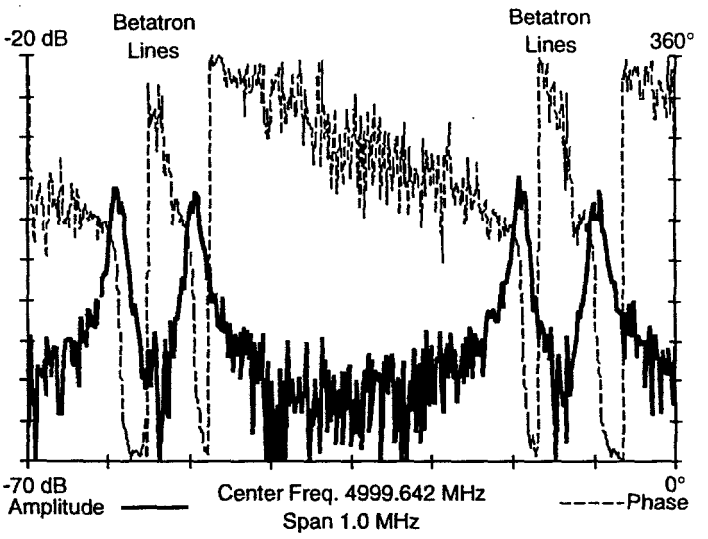


*Figure 11* The result of an open loop gain measurement of the FNAL debuncher transverse stochastic cooling system: A harmonic of the revolution frequency is at the center of the horizontal axis and the span covers almost two Schottky bands. The four peaks in amplitude *(solid curve)* occur at the four betatron sidebands (two per Schottky band). The betatron phase *(dashed curve)* shows at rapid 180° phase change at each betatron sideband.

example of the determination of $G$ over the bandwidth of a cooling system is shown in Figure 12. More details on experimental techniques in stochastic cooling are given by Marriner (36).

Momentum precooling is similar to betatron cooling except that a technique is required to develop a signal that is proportional to the momentum of the particle. The simplest technique is to place a difference pickup in a region of nonzero dispersion. The dispersion $\alpha_p$ is defined at any point in the ring by

$$\Delta x = \alpha_p \frac{\Delta p}{p}, \qquad 21.$$

where $\Delta x$ and $\Delta p$ are the position and momentum offsets, respectively. A pickup that measures the dipole moment of the beam in a region of dispersion will produce a Schottky voltage proportional to the momentum fluctuations in the beam. This voltage can be made to accelerate or decelerate the beam in an appropriate kicker and therefore cool the momentum spread. This cooling method is sometimes called the Palmer method.

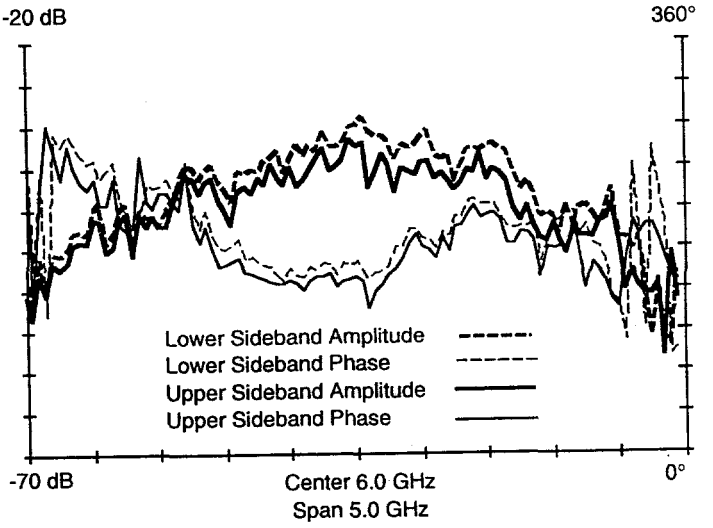


*Figure 12* The measurement of the open loop gain for the system shown in Figure 11, but only the peak response and phase at the peak response are shown for each Schottky band measured. The cooling gain function, including pickup and kicker response, is directly measured by this type of measurement.

A second technique is to use a notch filter. One type of notch filter is shown in Figure 13. Interference between waves in the short and long legs produces a response proportional to $1 - \exp(i\omega T_f)$, where $T_f$ is the transit time difference between the long and short legs. At any frequency that is a multiple $\omega = 2\pi n/T_f$, the response of the filter will be zero. The filter response will change sign depending on whether the particle revolution frequency is above or below the desired frequency $1/T_f$. This method is sometimes called the Thorndahl (37) method.

The two methods have disadvantages and advantages. The pickup placed in the region of dispersion will have poor signal-to-noise ratio (nominally zero) at the center of the pickup. The notch filter method avoids the low signal-to-noise ratio by filtering the noise as well as the signal, and the signal-to-noise ratio is (theoretically) constant throughout the notch. The filter method can only be used if the revolution frequency versus momentum relationship is unique (nonoverlapping Schottky bands). The filter also introduces undesirable phase characteristics that reduce the cooling rate. Thus, the filter method is used in situations where the signal-to-noise ratio is critical; otherwise the pickup in dispersion is used.

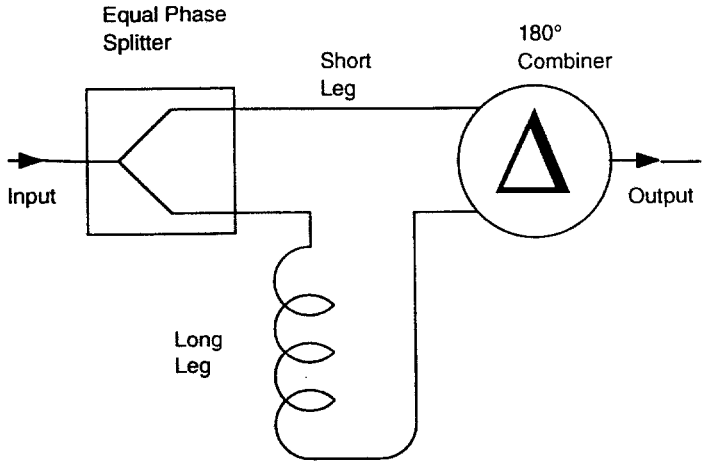


*Figure 13* A simple filter of the type commonly used for stochastic cooling is shown. The filter function arises from the interference of the waves in the short leg and the long leg.

## 10. MOMENTUM STACKING WITH STOCHASTIC COOLING

One of the most important components of the antiproton sources is the momentum stacking system. Momentum cooling is conventionally described in terms of the evolution of a distribution function with a Fokker-Planck type equation. Despite the different descriptive language, the cooling principles summarized in the previous section apply equally well to momentum stacking systems. Consider $N(E,t)$, the number of particles less than energy $E$ at time $t$. Define the flux $\Phi = \partial N/\partial t$ and the density $\Psi = \partial N/\partial E$. An equation analogous to Equation 17 can be written to describe the cooling process:

$$\Phi(E,t) = F(E)\Psi - [D_0 + D_1(E) + D_2(E)\Psi]\frac{\partial \Psi}{\partial E}. \qquad 22.$$

By using the relationship between momentum and frequency (Equation 12), $F$, $D_1$, and $D_2$ can be expressed as a sum over frequencies (harmonics of the revolution frequencies of the particles of energy $E$) in the cooling system. The flux is the rate at which particles are being added to the phase space between $E$ and $E + \Delta E$ and therefore represents the cooling rate. The first term, proportional to $F$, is the cooling term—the effect of a single particle on itself. The second term represents the heating effects: $D_2$ is the coefficient of the Schottky heating,

$D_1$ is the coefficient of the thermal heating, and $D_0$ contains all other sources of beam heating such as intrabeam scattering (discussed below). The coefficient $F$ is proportional to the system gain; $D_1$ and $D_2$ are proportional to gain squared, and $D_0$ is independent of system gain.

Neglecting for the moment $D_0$ and $D_1$, one can rewrite Equation 22 as

$$\Phi = -\frac{V}{T}\Psi - A\left(\frac{V}{T}\right)^2 \Psi \frac{d\Psi}{dE}, \tag{23.}$$

where $F = -V/T$ with $V = V(E)$ is the voltage gain per turn from the effect of the particle on itself (cooling) and $T$ is the time that the particle takes to make one turn. The dependence of $T$ on $E$ is small and can be neglected. The factor $A$ depends on $W$ (the system bandwidth), $\eta$, and $T$.

We consider a distribution $\Psi(E,t)$ where pulses of antiprotons are injected at large $E$ and accumulated at small $E$. At the injection energy $\Phi(E,t)$ is rapidly varying with time because of the pulsed injection. At the accumulation energy, the flux should decrease to zero. However, at intermediate energies we may expect to find a stationary solution with $\Phi(E,t) = \Phi_0 =$ constant. This solution corresponds to adding particles at a constant rate to a fixed area in phase space—exactly what is required for antiproton stacking. The function $V(E)$ can be tailored to obtain the maximum density increase with the smallest momentum aperture. From Equation 23, we can express the density gradient as

$$\frac{d\Psi}{dE} = -\frac{\Phi T^2}{AV^2\Psi} - \frac{T}{AV}. \tag{24.}$$

The gradient is maximized by differentiating Equation 24 with respect to $V$, setting the result to zero, and solving for $V$. The result is

$$V = -\frac{2\Phi_0 T}{\Psi}. \tag{25.}$$

Substituting Equation 25 into Equation 24 shows that the gradient is maximized everywhere when

$$\frac{d\Psi}{dE} = \frac{\Psi}{4A\Phi_0}. \tag{26.}$$

Thus the ideal profile is exponentially rising $\Psi \propto \exp(-E/E_d)$ with decreasing energy and the ideal gain (from Equation 25) is exponentially falling such that $\Psi(E)V(E) =$ constant. We have chosen the funda-

mental parameter $E_d = 4A\Phi_0$ to be positive for both CERN and FNAL, where the density increases with decreasing energy. The parameter $E_d$ is analogous to the coefficient $(W/N)^{-1}$ in Equation 17. A more detailed analysis shows that $A$ is effectively proportional to the momentum spread of the antiproton stack and inversely proportional to the bandwidth (11). Thus, the maximum antiproton flux is proportional to the bandwidth.

This design principle, requiring an exponential gain profile, is followed at both CERN and FNAL. A typical antiproton density profile from FNAL is shown in Figure 14. The density profile is obtained from a longitudinal Schottky pickup and plotted on a logarithmic scale by a spectrum analyzer. The distribution deviates from exponential near the left-hand side where the beam is injected. In this injection region the time dependence of $\Psi$ cannot be neglected. The injection and central regions are usually referred to as the stack tail. Figure 14 shows the distribution shortly after a pulse has been injected. The slope of the distribution increases significantly toward the right-hand side of the plot. This region is referred to as the stack core region or, more simply, the core. The increase in slope occurs primarily because of a separate core cooling system that operates with two times higher bandwidth.

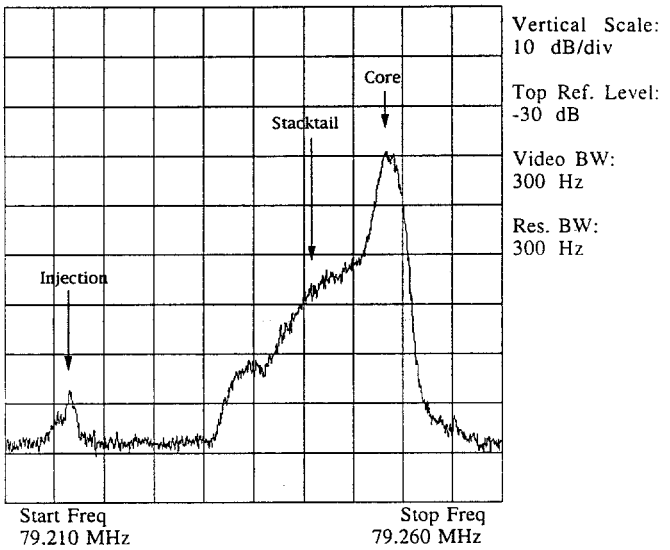


*Figure 14* A profile of the antiproton density during stacking at the FNAL antiproton source is shown. The profile is measured with a longitudinal pickup with a stack size of $2 \times 10^{11}$ antiprotons. The vertical scale is logarithmic.

which, for the same flux, produces a two times smaller value of $E_d$. The core cooling system produces a gain $F$ that changes sign around the desired position of the core and captures antiprotons around the energy where $F(E) = 0$. Figure 15 shows the design gain function $F(E)$ for the FNAL system. Both the stack tail and the core systems operate over the full energy range, but the core system dominates around $E = 0$, the stack tail elsewhere. The different abscissas in Figures 14 and 15 may be confusing. The particles are decelerated to higher revolution frequencies. The core is on the right in Figure 14 but on the left in Figure 15.

Two ways to obtain the gain function shown in Figure 15 are to use the gain shaping provided by pickups or to make the response of the electronics dependent on frequency. Any finite-sized pickup placed in a rectangular enclosure will have an asymptotic response proportional to $\exp(-\pi x/h)$, where $x$ is the distance from the pickup and $h$ is the box height of the enclosure, as illustrated in Figure 16. Pickups placed in the accelerator at a point where the dispersion is large, are sensitive to the beam energy. The exponential pickup response leads naturally to the desired exponential gain profile.

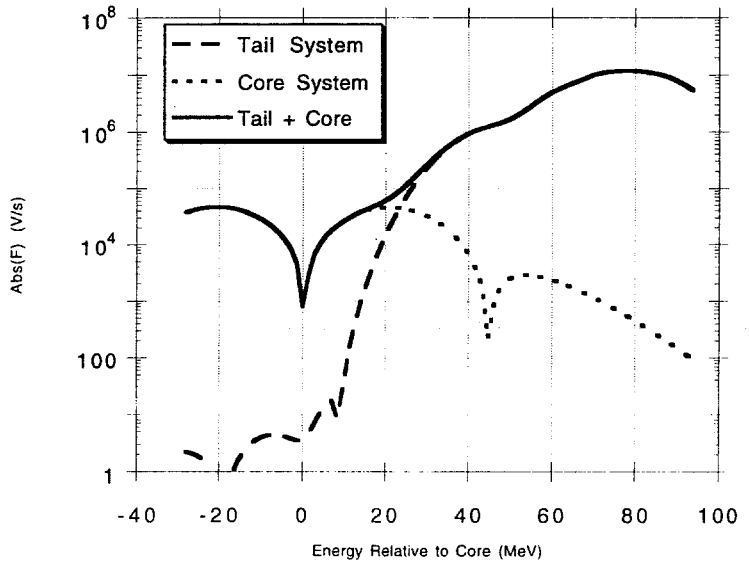


*Figure 15* This figure shows the design gain of the FNAL momentum stacking system. The total gain is negative for energies greater than zero and positive for energies less than zero.

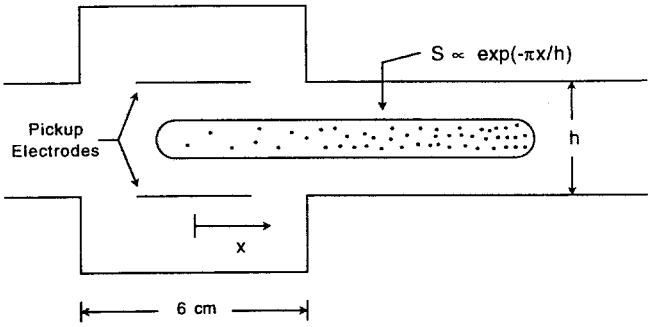


*Figure 16* A schematic representation of the FNAL stack tail pickup system and the stacked beam is shown. The pickup sensitivity is proportional to $\exp(-\pi x/h)$ at large $x$, where the beam density is high.

A single pickup with an exponential response can be shown to be inadequate from a consideration of the signal-to-noise ratio. The Schottky power in the cooling system is

$$P_s(\omega) \propto |G(\omega)|^2 \sum_{n=-\infty}^{\infty} \int \delta[\omega - n\omega_0(E)]|S(\omega,E)|^2 \Psi(E)\, dE, \qquad 27.$$

where $S(\omega,E)$ is the response of the pickup to the beam. The delta function picks out the frequencies generated by particles of energy $E$. The thermal noise power is

$$P_n(\omega) \propto |G(\omega)|^2 k_b(T_a + T_p), \qquad 28.$$

where $k_b$ is Boltzman's constant and $T_p$ and $T_a$ are respectively the temperature of the pickup and the amplifier noise (expressed in terms of equivalent temperature). The electronic gain $G(\omega)$ does not affect the signal-to-noise ratio. If the gain profile is obtained through the position sensitivity of the pickup, then $S(\omega,E) \propto \exp(E/E_d)$. Thus, the ratio of Schottky power to thermal noise power decreases with decreasing energy as $\exp(E/E_d)$. The ratio is unacceptable in the high density portion of the stack tail and the core region. The only known solution to the signal-to-noise problem is to use multiple sets of pickups centered at different energies. In this way the signal-to-noise ratio can be preserved for all energy particles. Both CERN and FNAL use two sets of pickups for the stack tail cooling system, and a third set for the core cooling system. The distinction between the stack tail and core cooling systems is somewhat arbitrary, except that the stack core sys-

tems have been chosen to operate at higher bandwidth for the increased cooling rate.

The different pickup systems operate at very different electronic gains. The gain must be greatest at the injection energy (in accordance with Equation 25) and smallest at the core. If no special measures were taken the thermal power of the high gain pickups would overwhelm the Schottky signal of the lower gain pickups. Thus, electronic gain shaping is required to reduce the thermal noise of the high gain pickups in the system. The gain shaping is accomplished with periodic notch filters (see Figure 13). Notch filters are designed to have zero response near harmonics of the revolution frequencies of the particles in the core.

The second possibility of obtaining the gain profile $V(E)$ is to use only the gain function $G(\omega)$. In this case $S(\omega,E) \approx$ constant, and the signal-to-noise ratio is independent of particle energy (avoiding the requirement for multiple pickups). However, consideration of the system stability shows that gain shaping with filters alone cannot work. The beam response function for longitudinal cooling can be described with an equation (see Equation 20) that involves a denominator of the form $1 - F_L(\omega)G(\omega)$, where $F_L(\omega)$ exhibits a resonant response at multiples of the rotation frequencies of the particles. However, the resonant response of the particles in the stack tail is completely dwarfed by the off-resonant response of the larger number of particles in the core. To obtain the optimum cooling, it is necessary that $G(\omega) \approx -1/\hat{F}_L(\omega)$, where $\hat{F}_L(\omega)$ refers to the resonant part of the beam response only. The previous solution, where the pickup sensitivity is energy dependent, namely $S(\omega,E) \propto \exp(E/E_d)$, avoids the stability problem by desensitizing the stack tail particles to the coherent response of the core.

## 11. INTENSITY AND DENSITY LIMITATIONS

One fundamental limitation on the achievable density comes from the random coulomb collisions among beam particles. This effect (39, 40), known as intrabeam scattering, results in beam emittance growth. In antiproton sources, intrabeam scattering calculations predict emittance growth in the horizontal and longitudinal motion and slow damping in the vertical. In practice, growth is also observed in the vertical amplitudes. The vertical growth is attributed to coupling between horizontal and vertical betatron motion. The rate of emittance growth from

intrabeam scattering is proportional to the number of particles present and depends in a complicated way on the beam size (smaller beams have faster growth rates). Other sources of heating are present and may be comparable in magnitude to intrabeam scattering. These sources include scattering from the residual gas and magnet power supply ripple. The growth rates for these latter phenomena are independent of the number of particles present ($d\epsilon/dt$ = constant). Both antiproton sources are believed to operate close to the intrabeam scattering limit, but unpublished data suggest that power supply ripple may dominate the growth rate at FNAL.

The cooling rate, according to Equation 17 or 19, is inversely proportional to the number of particles ($N$), whereas the heating rates are proportional to $N$ (intrabeam scattering) or independent of $N$ (power supply ripple). The cooling rate ($1/\epsilon\ d\epsilon/dt$) is independent of the emittance while the corresponding growth rates are at least inversely proportional to emittance. Thus, the equilibrium state, where the cooling rates and growth rates are equal, is sharply defined. Experimentally one observes equilibrium emittances in all three coordinates that grow approximately linearly with $N$. If the momentum spread of the stack core becomes sufficiently wide, as it eventually must, it will become impossible to stack additional beam. Either antiprotons will be lost because they fall outside the range of the core cooling system (because of the phase errors from bad mixing between pickup and kicker), or they will diffuse back into the stack tail cooling system and force the flux $\Phi(E,t)$ to zero because of the increasing $D_2\Psi$ term in Equation 22. Neither the CERN nor the FNAL source has operated with large enough stacks so that the momentum spread of the core has a major effect on the stacking rate.

Coasting beam instabilities can also limit the amount of stored beam in the accumulation ring. An instability results when the beam is displaced in some coordinate and the resulting force increases that displacement. Instabilities can be analyzed in terms of small amplitude oscillations with a time dependence of $\exp(-i\omega t)$. The amplitude will grow if $\omega$ has a positive imaginary part. Instabilities can be caused by self-forces within the beam, interaction with the walls of the beam chamber, or interaction with the residual ions trapped in the beam.

Instabilities due to wall impedances are well understood theoretically (41, 42). The effect of the vacuum chamber can be described in terms of a wall impedance. The resulting forces acting on the beam are proportional to the beam current. The impedance of the walls can be defined as the energy (or voltage) gained by the beam in a single turn divided by the beam current. The impedance is thus a property of the

structure of the vacuum chamber walls: it does not depend on the properties of the beam. The wall impedance can be analyzed in terms of its Fourier components $Z(\omega)$. The magnitude of the impedance determines the magnitude of the growth rate. The spread in oscillation frequencies of the individual particles in the beam provides a stabilizing mechanism known as Landau damping (43). The beam is unstable if the growth rate from the wall forces exceeds the Landau damping rate. A more detailed analysis shows that longitudinal instabilities can occur at frequencies that are near multiples of the revolution frequency, namely $n\omega_0$. A commonly used longitudinal stability criterion (41) is the Keil-Schnell criterion:

$$\left|\frac{Z(n\omega_0)}{n}\right| < K\frac{mc^2\beta^2\gamma|\eta|(\Delta p/p)^2}{ei_b}, \qquad 29.$$

where $K$ is a factor that depends on the beam distribution (but is of order 1), $\omega_0$ is the average revolution frequency, and $i_b$ is the beam current. The beam is stable provided that Equation 29 is satisfied for all integer values of $n$. The rf cavities, which have high impedances at their resonant frequencies, are potential violators of the stability condition and require special attention. With proper design techniques, the impedance of undesired resonant structures created by bellows or other enlargements in the transverse size of the vacuum chamber can be made small enough to avoid instabilities.

A similar criterion may be used for the stability of transverse motion:

$$\left|\frac{Z_\perp[(n-Q)\omega_0]}{n-\xi/\eta}\right| < 4K_\perp\frac{E}{e}\frac{\eta Q}{R\,i_b}\frac{\Delta p}{mc}. \qquad 30.$$

The transverse impedance $Z_\perp$ is defined as the ratio of the transverse-wall-induced forces (integrated over one turn) to the beam current times oscillation amplitude. The factor $K_\perp$ depends on the beam distribution; $R$ is the radius of the storage ring, and $E$ is the beam energy. Only frequencies in the neighborhood of the $n - Q$ betatron lines are unstable; the wall forces have a stabilizing effect on the $n + Q$ lines. Transverse instabilities caused by the resistance of the vacuum chamber walls are observed at both CERN and FNAL at the lowest value of $(n - Q)$. The instability is damped by feedback, which reduces the total destabilizing force.

The beam self-forces are not a serious problem for the antiproton sources, but ion forces are very much a problem. The antiproton beam ionizes the residual gas in the beam chamber. The ions have low energy

(about room temperature or 1/40 eV) compared to the electrostatic potential of the beam (tens of volts). These ions are therefore trapped in the potential well created by the beam. When the antiproton beam is displaced from the ion beam there is an electrostatic attractive force, which, if sufficiently strong, can lead to an instability (44).

A number of techniques have been used at CERN and FNAL to reduce the number of trapped ions. Ions born in the beam potential well oscillate transversely about the beam center. The transverse beam size varies around the storage ring, so the depth of the potential well and the oscillation frequency also vary. Ions will be accelerated toward a local minimum of the potential well. The first line of defense is a system of clearing electrodes to remove ions near the locations of the local minima of the potential well. Clearing electrodes are plates inserted into the vacuum chamber that produce a modest transverse dc electric field (a few kV/m) to sweep the ions from the beam. In the latter part of 1992, the FNAL source experienced significant problems with ion-induced instabilities. These problems were cured by an upgrade that increased the applied clearing voltage from 100 to 600 V, increasing the electric field from about 1 to 6 kV/m. A detailed account of clearing electrode technology at CERN has been given by Pederson et al (45). However, it is not possible to clear all the ions from a storage ring. Local pockets of ions may exist where there are no clearing electrodes. Ions born in regions where a magnetic field is present have relatively low drift velocities (proportional to $\mathbf{E} \times \mathbf{B}$) and may be the major cause of the ion instabilities observed at CERN (46).

The ion instabilities have been successfully avoided at the CERN antiproton source with the "beam shaking" technique. Briefly, a kicker excites coherent betatron oscillations of the antiproton beam at a frequency near—but slightly above or below—some harmonic of the betatron frequency $(n \pm Q)\omega_0$. Since the frequency is different than the betatron frequency, the antiprotons do not experience growth in their oscillation amplitudes. However, ions with oscillation frequencies equal to the driving frequency experience significant growth and are lost on the walls of the vacuum chamber when their amplitudes become large. Since the oscillation frequency of the ions varies around the storage ring, ions may travel in the longitudinal direction until their transverse motion is in resonance with the driving frequency. The effectiveness of the beam shaking technique is enhanced by the "lock on" effect (47) that results from the nonlinear motion of the ions. More details on the experience with ion effects and beam shaking are given by Marriner et al (48).

# 12. SETUP TECHNIQUES AND DIAGNOSTICS

Efficient operation of an antiproton source requires that a large number of parameters be set to appropriate values. Many useful diagnostics have been developed for use with low intensity antiproton beams. However, a wider variety of diagnostics can be used with higher intensity proton beams. Proton beams can be injected in the reverse direction via the antiproton extraction channel. In fact, it is routine procedure to check the extraction channel with reverse-direction protons while antiprotons are present in the core. Proton beams can also be injected into the antiproton source in the forward direction (bypassing the target) provided that the polarities of the magnets are reversed. Polarity reversal requires a significant effort and is done only during dedicated beam study periods. Forward and reverse protons can be used equally well to optimize apertures, measure and change betatron tunes, and adjust steering in beam lines. Critical timing of kickers, rf manipulations, and adjustments of stochastic cooling parameters require forward protons or antiprotons.

Many of the diagnostic devices used in antiproton sources are commonly used at high energy accelerators. Intensity measuring devices, such as toroidal beam current transformers, and beam profile measuring devices, such as segmented wire ion chambers (SWICs) or secondary emission monitors (SEMs), are used in beam lines to measure the beam intensity, position, and shape. Monitors that require the beam repeatedly to pass through matter (SEMs or SWICs, for example) cannot be used in storage rings because the beam would be quickly lost via nuclear interactions. The position of the beam in a storage ring is monitored by measuring the voltage difference between two pickup electrodes (a beam position monitor or BPM). The availability of proton beams in both normal and reverse directions makes possible a unique check that the phase space is properly matched in the transfers between the various storage rings. In a matched system, both forward and reverse beams will have the same position and size on all the position monitors in the system (provided that the respective proton beams have the correct initial positions and shapes). Beam scrapers are devices that can be remotely manipulated to restrict the beam aperture. They are used extensively to measure beam sizes and to infer aperture limitations.

As useful as proton beams are, antiproton sources spend most of their time producing antiprotons, and it is essential for them to have good diagnostics for low intensity beams. The antiproton beam as it

leaves the target is immersed in a sea of pions (which decay into muons) and electrons. Because of these particles, the secondary beam is of considerably higher intensity and is readily detected by the usual beam diagnostics. It is possible to use the pions, muons, and electrons effectively for beam tuning (49, 50). However, after a few tens of turns in the debunching ring, all particles except antiprotons are lost.

Possibly the most useful diagnostic device for the antiproton source is the Schottky pickup. Schottky signal measurements are particularly useful in antiproton sources because they are not destructive, are sensitive to coasting beams, and can be continuously monitored. A longitudinal pickup can detect both the beam intensity and its momentum distribution. Examples are shown in Figure 7 (bunch rotation) and Figure 14 (stacking). Schottky pickups can be sensitive to beams of as few as $10^6$ particles. Schottky pickup intensity measurements can be used to calculate the beam intensities at various stages in the antiproton source. An example is shown in Figure 17. The upper left histogram shows the beam intensity in the FNAL debuncher. The lower left histogram shows the bunch rotation efficiency, which is defined as the fraction of beam (after bunch rotation) within the momentum spread

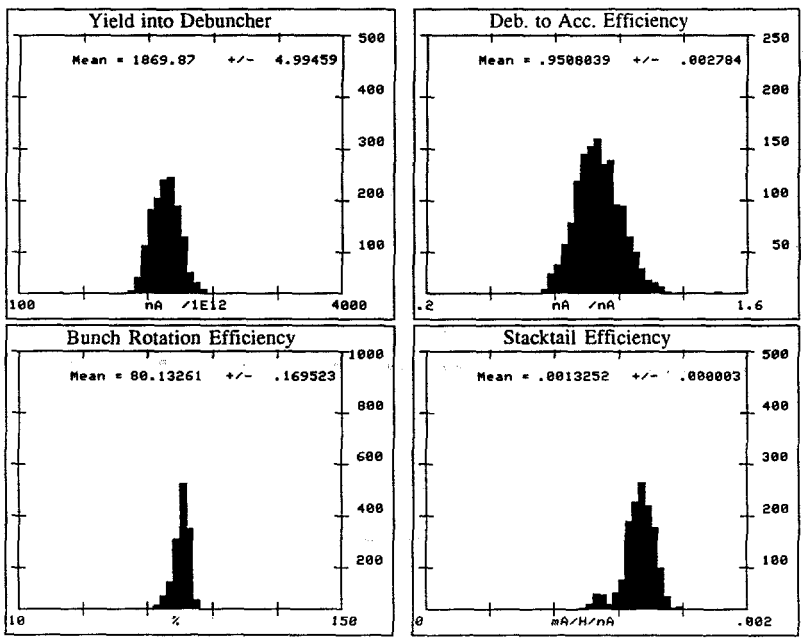


*Figure 17* Histograms of some of the quantities used to monitor antiproton source operation at FNAL are shown.

$\Delta p/p < 0.2\%$. The upper right histogram shows the fraction of beam transferred to the accumulator from the debuncher. Finally, the lower right histogram shows the stacking rate (in mA/hr) divided by the beam injected (per pulse) into the accumulator. This last histogram displays stacking efficiency (times the number of pulses per hour). One disadvantage of using Schottky signals is that coherent modulation of the beam, if present, will add to the Schottky signal and will cause an overestimate of the amount of beam present. This effect is small but noticeable in the FNAL debuncher.

The stacking rate is accurately measured from the increase in the direct current of the stored antiprotons. The current is equal to $Nef_0$ and is a measurement of $N$ since $ef_0$ is fixed. This measurement is useful because the current can be measured extremely accurately, typically (51) to 1 $\mu$A with a full scale range of 100 mA, i.e. one part in $10^5$. Thus, the accuracy of the current measurement is better than one pulse of antiprotons; the stacking rate can be measured to a few percent after 10 pulses. A typical plot of the stacking rate for the FNAL antiproton source is shown in Figure 18. Also shown on the plot are the Main Ring beam intensity and the horizontal and vertical emittances.

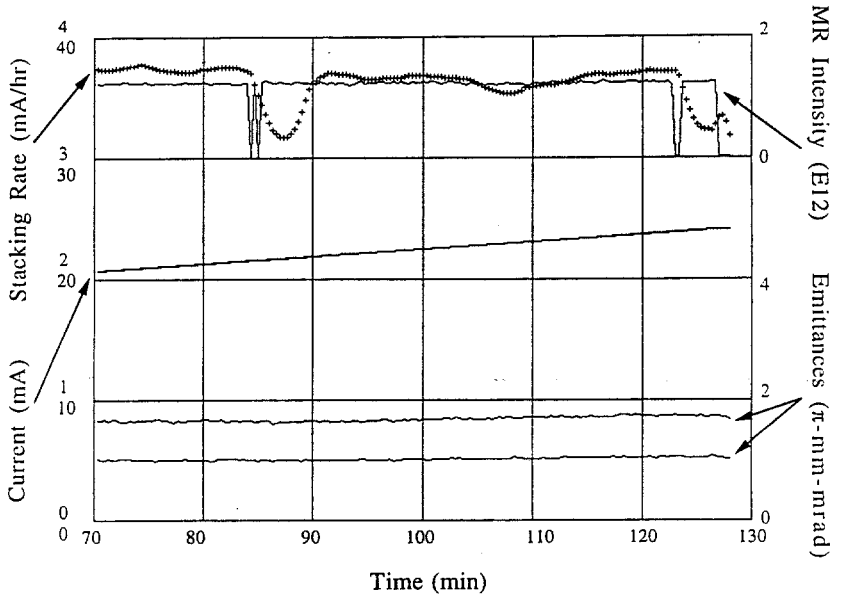


*Figure 18* A simplified version of the stacking rate display used at FNAL is shown. The stacking rate (+) is averaged over five minutes and shows decreases when the proton beam (MR Intensity) is interrupted. Also shown are the current and the horizontal and vertical emittance of the beam.

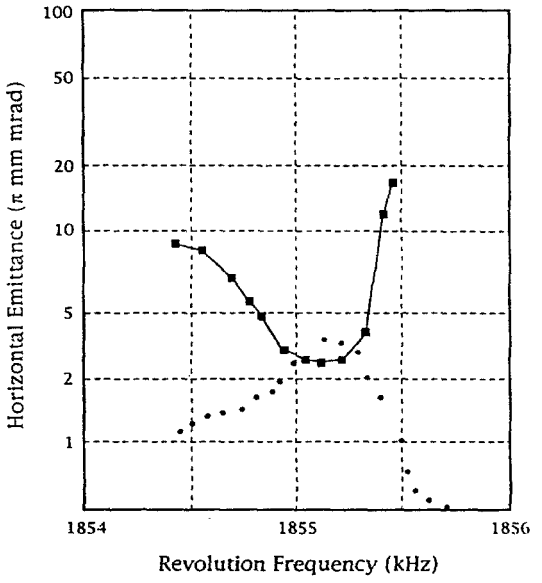


*Figure 19* A Schottky pickup is used to measure the horizontal emittance (*boxes*) vs revolution frequency at the CERN AA. The logarithm of the antiproton density is also shown (*dots*) with an arbitrary vertical scale.

Transverse Schottky signals are also used to measure the tunes, chromaticities, and emittances. The average emittance can be monitored with a Schottky pickup by measuring the total power from one of the sidebands and converting it into a voltage (52). This technique can track rapid changes in beam emittance. Another measurement with transverse Schottky signals is shown in Figure 19. The figure shows the emittance of the stack core beam in the CERN antiproton accumulator as a function of revolution frequency. The emittance changes as a function of frequency primarily because of the bad mixing between pickup and kicker. The data on this plot are used to adjust the timing of the transverse core cooling systems.

## 13. SUMMARY AND OUTLOOK FOR THE FUTURE

The antiproton sources built and operated at both CERN and FNAL have been extremely successful in terms of their technology and as tools to explore previously inaccessible domains of physics. The most outstanding of the particle physics discoveries has been the observation of the W and Z bosons.

The future of antiproton sources, however, is much less clear. Their major advantage is that they make it possible to convert fixed-target accelerators to colliding-beam machines. Their drawbacks are that they provide beams that are less intense than proton sources and that approach the intensity of proton beams only after long stacking periods. Furthermore, antiproton sources are expensive to build and operate.

The original antiproton sources had accumulation rates significantly below their design values (about a factor of five at both CERN and FNAL). This has served to underscore the impression that high luminosity proton-antiproton collisions were not possible. However, a major upgrade at CERN, minor improvements at FNAL, and a body of operational experience have led to stacking rates at both labs of about $4 \times 10^{10}$ antiprotons per hour. The originally projected luminosity of $10^{30}$ $cm^{-2}s^{-1}$ for proton-antiproton collisions has been exceeded by a factor of six. FNAL plans call for the improvement of its antiproton source and collider complex to achieve a luminosity of $5 \times 10^{31}$ $cm^{-2}s^{-1}$. CERN no longer operates with high energy proton-antiproton collisions, but maintains a program of lower energy physics at the LEAR facility. The FNAL program will presumably continue at least until the superconducting super collider (SSC) becomes available for physics experiments.

However, in the longer term, the future of the antiproton sources for high energy proton-antiproton collisions is not particularly bright. Future high energy hadron accelerators are being designed with the idea that they will either primarily or exclusively be used for colliding-beam physics. Thus, one is led to ask whether it is more advantageous to achieve high energy collisions with an antiproton source and a single ring or to build two rings to collide two proton beams. Particle physics arguments do not seem to heavily favor pp interactions over $\bar{p}p$ interactions (53). The cost of the second ring is partly offset by the cost of the antiproton source (54). Studies have indicated that one could design an antiproton source for the SSC that would accumulate $10^{12}$ antiprotons per hour and would support luminosities of $5 \times 10^{32}$ $cm^{-2}s^{-1}$ (55). At best this luminosity is comparable to the SSC design luminosity of $10^{33}$ $cm^{-2}s^{-1}$ for pp interactions. At worst it is a wildly optimistic proposal. Thus, the LHC (large hadron collider at CERN) and the SSC currently have no serious plans to incorporate antiproton beams.

The future of antiproton sources for lower energy particle physics is also unclear. The LEAR program may be terminated after the current program of experiments is completed in 2–3 years. The FNAL experiments with charmonium and possible future experiments will be considerably less viable without the need to provide antiprotons for high energy colliding-beam physics.

It is possible that the current applications of antiproton sources may become obsolete by the end of the decade. Whether that actually occurs or whether there will be new applications that require antiprotons, we do not know. However, we are confident that the techniques developed for antiproton beams and the understanding of these machines represent an important advancement in our understanding of accelerator science.

ACKNOWLEDGMENTS

We thank Carlos Hojvat, Mike Gormley, Dave McGinnis, and Steve O'Day for helpful comments. We also thank Dieter Möhl and Stephan Maury for providing information on the CERN antiproton source and LEAR.

*Literature Cited*

1. Rubbia C, McIntyre PM, Cline DB. In *Proc. Int. Neutrino Conf., Aachen, 1976*, pp. 683–87. Braunschweig, Germany: Vieweg (1976)
2. Budker GI. In *Proc. Int. Symp. on Electron and Positron Storage Rings, Saclay, 1966*, pp. II.1.1–II.1.5. Paris: Presses Universitaires (1966)
3. Budker GI, et al. *Part. Accel.*, 7:197–211 (1976)
4. van der Meer S. *CERN Internal Rep. CERN/ISR-PO/72-31* (1972)
5. Bramham P, et al. *Nucl. Instrum. Methods* 125:201–2 (1975)
6. Carron G, et al. *IEEE Trans. Nucl. Sci.* 24:1402–4 (1977)
7. Carron G, et al. *Phys. Lett.* 77B:353–54 (1978)
8. Carron G, et al. *IEEE Trans. Nucl. Sci.* 26:3456–61 (1979)
9. Autin B, et al. *CERN Internal Rep. CERN/PS/AA 78-3* (1978)
10. Wilson EJ, et al. *CERN Internal Rep. CERN 83-10* (1983)
11. Fermilab. *Design Report for Tevatron I Project*. Batavia, Illinois: Fermi Natl. Accel. Lab. (1984)
12. Plass G, et al. *CERN Internal Rep. CERN/PS/DL/80-7* (1980)
13. Armstrong TA, et al. *Phys. Rev. Lett.* 69:2337–40 (1992)
14. Bayanov BF, et al. *Proc. 10th Int. Conf. on High Energy Accelerators, Protvino, 1977*, 2:103–9 (1977)
15. Edwards DA, Syphers MJ. In *AIP Conf. Proc. 127: Physics of Particle Accelerators*, ed. M Month, PF Dahl, M Dienes, 1:1–61. New York: AIP (1985)
16. Hojvat C, van Ginneken A. *Nucl. Instrum. Methods* 206:67–83 (1983)
17. Taylor FE, et al. *Phys. Rev.*, D14: 1217–42 (1976)
18. Mokhov NV. *Sov. J. Part. Nuclei* 18: 408–26 (1987)
19. Azhgirey IL, Mokhov NV, Striganov SI. *Fermilab Tech. Memo TM-1529* (1988)
20. Azhgirey IL, Mokhov NV, Striganov SI. *Fermilab Tech. Memo TM-1730* (1991)
21. O'Day S, Visnjic V. *Fermilab Pbar Note 493* (1991)
22. Tang Z, Anderson K. *Fermilab Tech. Memo TM-1763* (1991)
23. Johnson CD, Jones E, Sherwood TR. In *Proc. 1987 IEEE Particle Accelerator Conf., Washington, 1987*, 3:1749–51. New York: IEEE (1987)
24. Dugan G. *Fermilab Pbar Note 467* (1986)
25. Dugan G, et al. *IEEE Trans. Nucl. Sci.* 30:3660–62 (1983)
26. Bellone R, et al. In *Proc. 8th Int. Conf. on High Energy Accelerators, Novosibirsk, 1986*, 2:272–75. Novosibirsk: Nauka (1986)
27. van der Meer S. *CERN Internal Rep. CERN/PS/AA/80-12* (1980)
28. Lambertson GR, Goldberg DA. In *AIP Conf. Proc. 249: The Physics of Particle Accelerators*, ed. M Month, M Dienes, 1:537–600. New York: AIP (1992)
29. van der Meer S. *CERN Internal Rep. CERN/PS/88-60 (AR)* (1988)
30. Evans BJ, et al. See Ref. 23, 3:1925–27
31. Griffin JE, et al. *IEEE Trans. Nucl. Sci.* 32:2806–8 (1985)
32. Boucheron J, et al. In *Proc. 2nd European Particle Accelerator Conf.*,

*Nice, 1990*, 1:958–60. Gif-sur-Yvette, France: Editiones Frontieres (1990)
33. Möhl D, et al. *Phys. Rep.* 58:73–119 (1980)
34. Marriner JP, McGinnis D. See Ref. 28, 1:693–761
35. Kirschman RK, ed. *Low Temperature Electronics*. New York: IEEE (1986)
36. Marriner JP. See Ref. 23, 3:1383–87
37. Carron G, Thorndahl L. *CERN Internal Rep. CERN-ISR-RF/78-12* (1978)
38. van der Meer S. *CERN Internal Rep. CERN/PS/AA/78-22* (1978)
39. Piwinski A. In *Proc. 9th Int. Conf. on High Energy Accelerators, Stanford, 1974* pp. 405–9. Stanford, Calif: SLAC (1974)
40. Bjorken JD, Mtingwa S. *Fermilab Internal Rep. Fermilab-Pub-82/47-THY* (1982)
41. Hofmann A. In *CERN Internal Rep. CERN 77-13*, ed. MH Blewett, p. 139 (1977)
42. Zotter B. See Ref. 41, p. 176
43. Hereward, HG. See Ref. 41, p. 219
44. Alves-Pires R, et al. In *Proc. 1989 IEEE Particle Accelerator Conf. Chicago*, 2:800–2. New York: IEEE (1989)
45. Pederson F, Poncet A, Soby L. See Ref. 44, 3:1786–89
46. Carron G, et al. See Ref. 44, 2:803–5
47. Orlov Y. In *Proc. on Crystalline Ion Beams, Wertheim, 1988*, pp. 133–39. Wertheim, Germany (unpublished)
48. Marriner JP, et al. In *Proc. 1989 Int. Conf. on High Energy Accelerators, Tsukuba, 1989*, pp. 971–78. New York: Gordon & Breach (1989)
49. Johnson CD, et al. *IEEE Trans. Nucl. Sci.* 32:3000–2 (1985)
50. Johnson CD, et al. *IEEE Trans. Nucl. Sci.* 30:2821–23 (1983)
51. Unser K, et al. *IEEE Trans. Nucl. Sci.* 28:2344–46 (1981)
52. Peterson DP. In *Proc. 2nd Annu. Workshop on Accelerator Instrumentation, Batavia, 1990*, ed. ES McCrory, pp. 108–30. New York: AIP (1991)
53. Paige F. In *DPF Proceedings: $P\bar{P}$ Options for the Supercollider*, ed. JE Pilcher, AR White, pp. 1–54. Chicago: Univ. Chicago, Argonne Lab. (1985)
54. Barish BC, et al. *SSC Internal Rep. SSC-SR-1022* (1986)
55. Simpson J, et al. See Ref. 53, pp. 301–85